AIMS Energy, 14(3): 472–493.
DOI: 10.3934/energy.2026020
Received: 06 January 2026
Revised: 24 March 2026
Accepted: 20 April 2026
Published: 08 May 2026

https://www.aimspress.com/journal/energy

Research article

Investigating the dual impact of multi-selected electrode thicknesses and channel heights for optimal performance in vanadium redox flow batteries

Mohammed A. Al-Yasiri*

Mechanical Department, College of Engineering, Wasit University, Kut 52001, Iraq

* **Correspondence:** Email: maapbd@uowasit.edu.iq; Tel: +9647818331394.

Abstract: The performance of vanadium redox flow batteries (VRFB) is affected by multiple factors, such as flow field design and electrode size. Providing a smooth electrolyte supply to a suitable electrode size is determinant for battery performance. In this work, the dual impact of channel height and electrode thickness on overall battery efficiency (in nine different combinations) was investigated numerically through a 3D model involving electrolyte motion. The individual role and the dual impact of both factors on electrolyte penetration into the electrode, overpotential, and pressure losses were evaluated to highlight how these affect the output charge-discharge voltages, optimal flow rate, energy efficiency, and overall system efficiency. Numerous operating conditions, like state of charge (SOC), volumetric flow rate, and current density, were implemented to identify the most efficient cell combination among the studied cases. In general, the voltage response is improved as the channel height is reduced and/or electrode thickness is increased due to the reduction in overpotential; however, large pump losses are also produced. A balance between enhanced voltage and pumping power increment is required to achieve maximum battery efficiency (at optimal flow rate), depending on the cell configuration and applied conditions. Results indicate that channel height has a positive effect on energy efficiency at low flow rate, more so than electrode thickness, whereas the opposite is noticed at high flow rate. Additionally, for the best battery efficiency, electrode thickness is more determinant, followed by channel height, based on operating conditions. Overall, case 7 (smallest channel height and largest electrode thickness) performed best in terms of energy/battery efficiency at a relatively low optimal flow rate, whereas case 3 (largest channel height and smallest electrode thickness) performed worst; however, this effect is lowered at high current density. This model can guide the design of optimal flow batteries and loading conditions.

Keywords: electrode and channel dimensions; optimal flow rate; overall efficiency enhancement; electrolyte penetration into electrodes; 3D model of a single VRFB cell

1. Introduction

Classical energy sources such as natural gas, oil, and coal are limited and have a negative impact on the environment and human life, mainly due to the emissions of CO_2 and greenhouse gases that cause climate change [1]. This has motivated researchers to explore alternative clean sources, like solar and wind energy, as renewable sources to serve two objectives: (1) transitioning from non-renewable toward sustainable energy sources, and (2) achieving the increasing energy demand [2,3]. Improving smart grid stability and reliability requires using energy storage technologies that mitigate the drawbacks of renewable sources, i.e., intermittency and uncertainty. Redox flow batteries (RFBs) are electrochemical energy storage devices that convert electricity into chemical energy, and vice versa, through redox reactions [4,5]. Flow batteries exhibit advantages over conventional batteries, including their ability to decouple output power from energy capacity, improved safety, scalability of energy capacity, longer cycle life, and less capacity degradation over time, which lead to a more flexible design for specific applications [6,7]. Among a wide range of flow batteries, vanadium redox flow batteries (VRFBs) have more applications since they use the same chemical species on both sides. At the cathode and the anode, vanadium is utilized in different oxidation states, which prevents contamination due to vanadium crossover ions through the membrane [8,9]. Developing novel materials, including improved ion-exchange members, electrolyte solutions, and porous electrodes, and improving design parameters, such as flow field configurations and electrode shapes, improves VRFB cost reduction and demand [10,11].

Flow field design plays a crucial role in enhancing overall flow battery performance. The flow field architecture ensures an even distribution of electrolyte, current, and potential at the electrode surfaces, which prevents the formation of dead zones and high local current densities, also functioning as an electron conduction medium [12,13]. Maintaining a uniform liquid distribution can be achieved by either increasing the flow rate, which leads to high consumed pumping power and overall battery reduction [14,15], or utilizing a flow field pattern located between the electrode and the current collector, which reduces pump losses to a reasonable amount [16,17]. The latter approach is well-established in the literature on fuel cell technology, where numerous types of flow field configurations have been introduced and examined. Additionally, in VRFBs, increasing electrode thickness can play two roles: (1) providing more active area for electrochemical reactions leading to improved overall battery performance, and (2) introducing challenges related to mass transport, including ion diffusion and electron movement, pressure drop, resistance increment, and the possibility of mechanical instability [18,19]. Thus, for optimal design of a VRFB system, it is essential to study the impact of these two factors, i.e., flow field and electrode thickness, on the VRFB performance.

Many studies have investigated VRFB performance considering different channel shapes and electrode materials. However, these mainly focused on different channel configurations (parallel, interdigital, spiral, and serpentine) and cathode and anode thickness/materials. The voltage response of several electrode/electrolyte materials was investigated numerically through a 2D sensitivity analysis model [20], and it was found that voltages were only determined by the conductivity of the electrolyte and electrode, electrode porosity, and specific surface area. In Reference [21], an experimental study was conducted to evaluate three different flow fields using felt electrodes compared with a serpentine flow geometry utilizing carbon paper electrodes under the same operating conditions. The highest energy efficiency was 75% for the conventional flow field type and 64% and 55% for the serpentine and interdigitated types, respectively. A 3D numerical model was developed and validated experimentally to investigate, numerically and experimentally, the effect of a single interdigitated and serpentine flow field in a half-cell VRFB with 25 cm^2 active area. Higher pumping losses and better battery performance were obtained with a single serpentine flow field compared to an interdigitated flow field at the same operating conditions [22]. In Reference [23], the impact of channel and/or rib dimension was experimentally evaluated on pressure drop and electrochemical performance of a serpentine geometry. By studying eight channels and/or rib dimensions in cells of 400 and 900 cm^2 active area, a noticeable improvement in pressure drop was observed in the larger cell, and better performance was obtained when the channel and rib widths were increased and decreased, respectively. In Reference [24], a new structure of a single VRFB was fabricated and tested, employing non-porous and non-brittle bipolar plate materials to compensate for the carbon composite in conventional cells. The novel cell eliminated components like insulators, gaskets, and end plates, which helped to improve cell assembly, safety, weight, lifespan, and cost. Three different electrodes (a conventional electrode, a variable cross-section electrode with one side placed interdigitally, and a variable cross-section electrode with two sides placed interdigitally) were implemented through a 3D numerical model to predict the VRFB performance in Reference [25]. The third electrode demonstrated 1.25% higher discharge voltage than the second one. Uniformity factors were 14.24% and 19.56% for the second and third electrodes, respectively, higher than that of the conventional one. According to the numerical model results, the second electrode showed the best performance in terms of charge-discharge voltages and overpotential. In Reference [26], a circular cross-section electrode was introduced as an alternative to a rectangular one to enhance mass transfer and reduce concentration polarization. Results showed an increment in electrolyte consumption of 10.52% and an improvement in energy storage capacity of 12.56% at 40 mA/cm^2; performance was improved at higher current densities. The combined effect of two electrode thicknesses (1 and 4 mm) and porosity of a serpentine flow field on VRFB performance was also investigated numerically [27]. There was an increment in discharge voltage as the flow rate and porosity increased. Also, for the 1 mm electrode thickness, the maximum power-based efficiency was 96.8% at 10 mL/min; for the 4 mm electrode thickness, it was 96.4% at 50 mL/min. The maximum output current and charge-discharge voltage responses in VRFB were predicted by implementing a 2D numerical model with a range of parameters such as porosity, state of charge (SOC), volumetric flow rate, and current density. Increasing flow rate, porosity, and SOC resulted in maximum output current and voltage response increments [28]. In Reference [29], a 3D model of seven electrode shapes with the same volume (10 cm^3) was conducted to investigate VRFB energy and overall battery efficiencies under a range of SOC. Results indicated that thicker electrodes suffered from poor performance due to reduced electrolyte distribution and electrochemical reactions. A novel double-spiral channel flow field design with inlets and outlets at the center has been introduced to evaluate the overall performance of a single VRFB cell [30]. The results of this design were compared with classical flow field designs, i.e., serpentine and interdigitated, and superior outcomes were achieved. At 100 mL/min, the pressure drop in the new design was reduced by 33% compared to the serpentine flow field geometry, together with a higher discharge voltage and an enhancement in system efficiency. Overall, the double-spiral channel flow field design with outlets at the center performed better than the one with inlets at the center (e.g., 13.8% higher in peak power density). The uneven electrode deformation due to stack assembling and mechanical stress has been studied through a 3D numerical model to investigate VRFB performance [31]. Different compression ratios were simulated for three flow field designs by adjusting gasket thickness. Results indicated that concentration overpotential and pressure drop were more affected by the compression ratio than by the concentration uniformity. At a compression ratio 40%–50%, minimum overpotential was determined by the flow field design: A 45% compression ratio was considered optimal for an interdigitated flow configuration.

For the last few decades, VRFB performance has been investigated, aiming at its development for commercialization and industrial adoption. Prior studies have mostly focused on improving energy and/or battery efficiency through factors such as electrode and membrane materials, vanadium electrolyte concentration, and flow channel configurations (e.g., serpentine, interdigital, parallel, and spiral). However, important questions remain regarding the combined (dual) impact of electrode thickness and channel height on battery performance, particularly as functions of flow rate and current density. In this work, the focus was to investigate the coupled effects of electrode thickness and channel height on overall battery performance. Three different values were selected for both parameters, all within experimentally and literature-supported ranges. To the best of the authors' knowledge, this combined analysis has not been previously reported. The findings presented in this study provide valuable insights and practical guidance for optimizing flow battery design and operating conditions.

2. Numerical model development

2.1. Model building structure

A schematic view of a single VRFB cell is depicted in Figure 1a, consisting of a combination of two porous electrodes, two external tanks to store or extract electrical energy, two pumps to circulate vanadium solutions on both sides, a membrane, a DC/AC inverter, and a current collector. The simulated domains in this model are two porous electrodes, a membrane, and two flow channels, as illustrated in Figure 1b. Nine combinations (cases) of three different electrode thicknesses (H_E) and channel (H_C) heights are considered, as listed in Table 1.

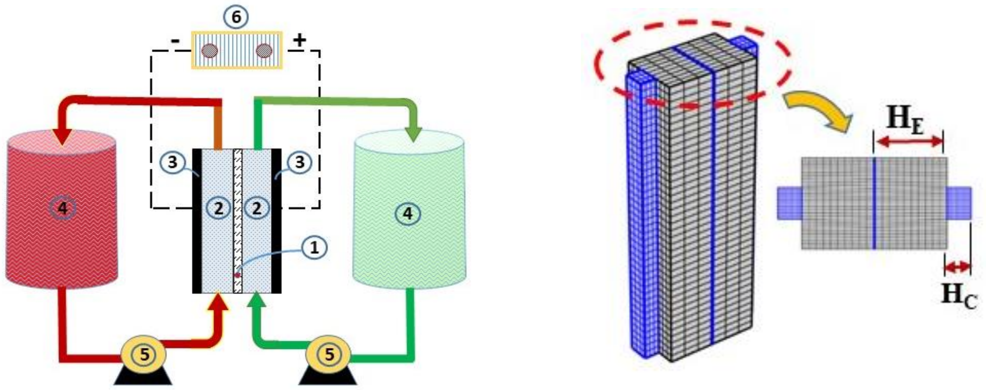

(a) (b)

Figure 1. (a) Schematic of a single flow cell: (1) membrane, (2) anode and cathode, (3) current collectors, (4) electrolyte tanks, (5) pumps, (6) DC/AC inverter. (b) 3D geometry mesh.

Table 1. Dimensions of the nine studied combinations (cases) for VRFB.

Channel height (H_C)	Electrode thickness (H_E)		
	6 mm	4.5 mm	3 mm
	Nine studied cases		
2 mm	Case 1	Case 2	Case 3
1.5 mm	Case 4	Case 5	Case 6
1 mm	Case 7	Case 8	Case 9

2.2. Model assumptions

The current model focuses on essential performance metrics, such as cell voltage, power, and state of charge (SOC); the following assumptions are considered: (a) operating the cell in moderate conditions (10–40 °C) does not drastically change vanadium solution properties like conductivity, allowing an average constant temperature to be assumed; (b) incompressible electrolyte liquid (small change in the solution volume); (c) no side reactions (no generation of hydrogen and oxygen); (d) isotropic properties of charge and mass transfer in the porous electrode, membrane, and vanadium species (no spatial position change); (e) no penetration of ions and water through the membrane [using modern, highly selective ion exchange membranes (IEMs) that are specifically designed to be highly permeable to protons (to maintain charge balance) but impermeable to vanadium species and water]; (f) dilute solution (low ionic concentration of vanadium species compared to water); (g) no leakage of reactant and charge through the external surfaces of the cell; and (g) pseudo steady state (big reservoir compared to the inner volume of the electrolyte).

2.3. Model formulation

Chemical reactions in VRFB are based on the oxidation and reduction of vanadium species that occur at the interfaces between the electrolyte and the solid structure. The general electrochemical reaction equation is as follows:

$$V^{4+} + H_2O + V^{3+} \xLeftrightarrow{discharge-charge} V^{5+} + V^{2+} + 2H^{+} \tag{1}$$

At the cathode (catholyte):

$$V^{4+} - e^{-} \xLeftrightarrow{discharge-charge} V^{5+} \tag{2}$$

At the anode (anolyte):

$$V^{3+} + e^{-} \xLeftrightarrow{discharge-charge} V^{2+} \tag{3}$$

Based on the principle of conservation, the governing equations are applied on five domains, i.e., the anode and cathode as a porous medium, the membrane, and two flow channels as free media. In the flow channel region, momentum and continuity are described by the Navier–Stokes (NS) equations for incompressible flow [32]:

$$\rho(\vec{u}.\ \nabla)\vec{u} \ = -\nabla p + \nabla[\mu \ \cdot (\nabla\vec{u} + (\nabla\vec{u})^T)] + \vec{f} \tag{4}$$

$$(\nabla \cdot \vec{u}\,) = 0 \tag{5}$$

where the symbols $\rho, u, \nabla p, f, and\ \mu$ represent electrolyte solution density, species velocity, pressure gradient, volume force vector, and vanadium solution dynamic viscosity, respectively. For the flow in porous media, the corresponding equations are presented by the Brinkman equation as follows:

$$\frac{\rho}{\varepsilon}\,(\vec{u}\cdot\nabla)\frac{\vec{u}}{\varepsilon} = -\nabla p + \nabla\cdot\left[\frac{\mu}{\varepsilon}\,(\nabla\vec{u} + (\nabla\vec{u})^T)\right] - \frac{2\mu}{3\varepsilon}\nabla(\nabla\cdot\vec{u}\,) - \left(\frac{\mu}{K} + Q\right)\vec{u} + \vec{f} \tag{6}$$

$$(\nabla \cdot \vec{u}) = 0 \tag{7}$$

where $Q\ and\ K$ refer to the mass source and permeability of porous electrode, respectively; the latter can be evaluated by the Carman–Kozeny equation [33]:

$$K = \frac{d_f^2\ \varepsilon^3}{16C_k\,(1-\varepsilon)^2} \tag{8}$$

where d_f, C_k are the fiber diameter and the Carman–Kozeny constant that is used as a fitting parameter depending on the media type.

The modified Nernst–Planck equation is applied to describe ion flux and charge transport in an electrolyte flow through a porous electrode as a result of diffusion, migration, and convection (influence of various forces), as shown below [33]:

$$\vec{N}_{i,e} = \ -D_i^{eff}\ \nabla C_{i,e} - \ Z_i\, M_{i,e}\, C_{i,e}F\ \nabla\emptyset_{l,e} + \ \vec{u_i}\ C_{i,e} \tag{9}$$

where $\vec{N}$ is the molar flux of the species in the electrolyte (species of i subscripted by e $\{V^{2+}$, V^{3+}, V^{4+}, V^{5+}, HSO_4^-, and $H^+\}$), $M_{i,e}$ is the ionic mobility in the electrolyte, $\emptyset_{l,e}$ is the ionic potential, F is the Faraday constant, $C_{i,e}$ is the species concentration, Z_i is the species valence, and D_i^{eff} is the effective diffusion coefficient calculated by the corrected Bruggemann equation [33]:

$$D_i^{eff} \ = \ D_i\ \varepsilon^{1.5} \tag{10}$$

where ε refers to the electrode porosity. The mobility of ions, $M_{i,e}$, is defined by the Nernst–Einstein equation under the dilute solution approximation [34]:

$$M_{i,e} = \frac{D_i^{eff}}{R\,T} \tag{11}$$

where $T(298\ K)$ is the temperature, and $R\left(8.314\ \frac{J}{mol.K}\right)$ is the universal gas constant.

The conservation of species in Eq (9) can be written as [35]:

$$\nabla.\, N_{i,e} = R_{i,e} \tag{12}$$

where $R_{i,e}$ represents the source term of species in the porous electrode, i.e., V^{2+}, V^{3+}, and H^+ at the anode and $V^{4+}$and V^{5+} at the cathode [36].

The porous electrode region shows electrochemical reactions, species transport, and transfer of current, which can be expressed by the charge conservation equation as follows:

$$\nabla \cdot \vec{J_l} = -\nabla \cdot \vec{J_s} \tag{13}$$

where $\vec{J_l}, and\, \vec{J_s}$ refer to the total solid current density in the anode and the cathode, respectively, across the membrane.

The total electrolyte current density in the porous electrode can be formulated after applying the electroneutrality equation:

$$\vec{J_l} = -K^{eff}\,\nabla\emptyset_{l,e} - F\,\sum_i Z_i\, D_i^{eff}\,\nabla C_{i,e} \tag{14}$$

where K^{eff} is the effective conductivity given by

$$K^{eff} = \frac{F^2}{RT}\sum_i Z_i^2\, D_i^{eff}\, C_{i,e} \tag{15}$$

Ohm's law is used in the porous electrode to determine the electronic potential, $\emptyset_{s,e}$, as follows:

$$\vec{J_s} = \sigma_s^{eff}\nabla\emptyset_{s,e} \tag{16}$$

The Bruggeman equation is applied to find the electrode effective conductivity, σ_s^{eff}, based on the solid material conductivity, σ_s, as follows:

$$\sigma_s^{eff} = (1-\varepsilon)^{3/2}\,\sigma_s \tag{17}$$

Butler–Volmer formulation is applied to evaluate the local current densities at the anode and the cathode [36]. The equilibrium potential (open circuit voltage) for negative ($E_{0,neq}$) and positive ($E_{0,pos}$) reactions is described below.

$$E_{0,neq} = E^S_{0,neg} + \frac{RT}{F}\,ln\left(\frac{C_{3,e}}{C_{2,e}}\right) \tag{18}$$

$$E_{0,pos} = E^S_{0,pos} + \frac{RT}{F}\,ln\left(\frac{C_{5,e}\cdot\left(C_{H,pos}\right)^2}{C_{4,e}}\right) \tag{19}$$

$E^S_{0,neg}$ and $E^S_{0,pos}$ represent the standard reduction potentials for the negative and positive electrodes, respectively.

Estimating the state of charge related to the open circuit voltage, V_{OCV}, is as follows [37]:

$$V_{OCV} = V^o_{OCV} + \frac{RT}{nF}ln\frac{(SOC)^2}{(1-SOC)^2} \tag{20}$$

where the standard open circuit voltage (V^o_{OCV}) at 50% SOC is 1.4 V.

The concentrations of vanadium species at any time can be converted to the state of charge (SOC), as follows [35]:

$$SOC = (S_e - S_o)\frac{t}{t_t} + S_o \tag{21}$$

where $S_e, S_o, t_t, and\ t$ represent the initial SOC, the final SOC, the total charging/discharging operating time, and the corresponding time of SOC, respectively.

In this simulation, the side reactions and ion diffusions or water transport across the membrane are neglected, i.e., a balanced electrolyte. The expressions of reactant and product concentrations as a function of SOC are:

$$\begin{cases} C^{V+2} = C^{V+5} = C^{Vt}.SOC \\ C^{V+3} = C^{V+4} = C^{Vt}.(1 - SOC) \end{cases} \tag{22}$$

where C^{V+2}, C^{V+3}, C^{V+4}, and C^{V+5} refer to the concentration of species V^{+2}, V^{+3}, $V^{+4}, and\ V^{+5}$, respectively, and $C^{Vt} = 1040$ mol·m^{-3} is the total concentration of the negative and positive electrodes.

2.4. Boundary conditions

For the conservation of momentum, no leakage of electrolytes through the surfaces is assumed. Also, a Neumann condition ($\nabla p \cdot \vec{n} = 0$) at the boundaries of the electrode domain is applied to satisfy the electrolyte pressure. A fully-developed flow approximation is considered at the outlets, where the liquid pressure and all reactant diffusive fluxes are set to zero ($P = P_{out} = 0$ and $D_i^{eff}\ \nabla C_{i,e} = 0$). At the inlet of the inflow channel, the velocity condition is equal to $V = Q/A_c$, where Q and A_c refer to the volumetric flow rate and channel inlet cross section area, respectively. No vanadium species and electron fluxes penetrate the membrane ($\nabla N_{i,e} \cdot \vec{n} = 0$ and $\nabla \emptyset_s \cdot \vec{n} = 0$), except protons. At the electrode/collector interface, the electronic potential flux condition during charge is $-\sigma_s^{eff}\ \nabla \emptyset_s \cdot \vec{n} = -I/\alpha$, where I is the applied current (with either positive or negative), and α is the surface area of the electrode. At the electrode–membrane interface, the ionic potential flux condition during charge is $-K^{eff}\ \nabla \emptyset_{l,e} \cdot \vec{n} = I$, whereas insulated conditions for the rest of the electrode surfaces are applied ($-\vec{n} \cdot \vec{J_l} = -\vec{n} \cdot \vec{J_s} = 0$). At the anode (negative electrode), the solid potential is set to zero as a reference potential for the remainder of the cell ($\emptyset_s = 0$).

The expressions of species concentration at the channel inlet are expressed to the status of SOC = 15%, as follows [34]:

$$\begin{cases} {C_{in}}^{2,5} = C^{Vt} \cdot SOC \\ {C_{in}}^{3,4} = C^{Vt} \cdot (1 - SOC) \\ {C_{in}}^{H+} = C^{Vt} \cdot SOC + CH_{H+}^{in,pos} \\ {C_{in}}^{H-} = C^{Vt} \cdot SOC + C_{H-}^{in,neg} \end{cases} \tag{23}$$

Table 2 presents the electrochemical properties, operating parameters, and dimensions utilized in the simulations.

Table 2. Electrochemical properties, operating parameters, and cell dimensions used in the simulations.

Parameter	Value	Parameter	Value
Electrode length	40 (mm)	Anolyte density	1300 $(kg \cdot m^{-3})$
Electrode width	11.5 (mm)	Catholyte density	1350 $(kg \cdot m^{-3})$
Electrode thickness	From Table 1	V^{2+} initial concentration in anolyte	156 $(mol \cdot m^{-3})$
Membrane thickness	0.203 (mm)	V^{3+} initial concentration in anolyte	884 $(mol \cdot m^{-3})$
Rib width	7.5 (mm)	V^{4+} initial concentration in catholyte	884 $(mol \cdot m^{-3})$
Channel height	From Table 1	V^{5+} initial concentration in catholyte	156 $(mol \cdot m^{-3})$
Channel width	4 (mm)	H_{neg}^{+} initial concentration in anolyte	4447.5 $(mol \cdot m^{-3})$
Operating temperature	25 $(°C)$	H_{pos}^{+} initial concentration in catholyte	5097.5 $(mol \cdot m^{-3})$
Current density	33.33–133.33 $(mA.cm^{-2})$	V^{2+} diffusion coefficient	2.4×10^{-10} $(m^2 \cdot s^{-1})$
Volumetric flow rate	3–125 $(mL \cdot min^{-1})$	V^{3+} diffusion coefficient	2.4×10^{-10} $(m^2 \cdot s^{-1})$
Outlet pressure	0 (pa)	V^{4+} diffusion coefficient	3.9×10^{-10} $(m^2 \cdot s^{-1})$
Porosity	0.9	V^{5+} diffusion coefficient	3.9×10^{-10} $(m^2 \cdot s^{-1})$
Fiber diameter	50.3 (μm)	Proton diffusion coefficient	9.312×10^{-9} $(m^2 \cdot s^{-1})$
Electrode electronic conductivity	66.7 (S· m^{-1})	HSO_4^- diffusion coefficient	1.33×10^{-9} $(m^2 \cdot s^{-1})$
Standard potential for anode	−0.255 (V)	SO_4^{2-} diffusion coefficient	1.065×10^{-9} $(m^2 \cdot s^{-1})$
Standard potential for cathode	1.004 (V)		

2.5. Case simulation

In the current work, nine combinations (cases) of different channel heights and electrode thicknesses were simulated, as listed in Table 1. All simulations were implemented at the same operating conditions, based on the literature: volumetric flow rates (5, 25, 75, and 125 mL/min), current densities (33.33, 83.33, and 133.33 mA/cm^2), and state of charges (SOC) (0.15–0.95) through the charge-discharge curves. Pre-established limits of cutoff voltage were set during the charge-discharge process. The state of charge was increased during the charge process (SOC 0.15–0.15), or the cell voltage reached 1.7 V. On the other hand, the VRFB was discharged when the state of charge decreased (SOC 0.95–0.15) or the cell voltage dropped to 0.95 V. The validity of the aforementioned statement, however, could not be satisfied under operating conditions of high current density and/or low flow rate.

3. Results and discussion

3.1. Numerical details and grid independence test

In the current model, the conservation equations were solved using the COMSOL Multiphysics® package using a finite-element method. A quadratic basis was used, including cell refinement within the membrane close to the electrode–membrane interface with a relative error of 10^{-5}. A grid convergence study was implemented to ensure the robustness of the results as the number of mesh elements increases. Figure 2a presents the discharge voltage for the cell (case 7) under four different meshes of 405, 810, 1620, and 3240 elements with a total degree of freedom of 6698, 12,278, 23,438, and 45,758, respectively. The same simulation conditions were employed, except for the number of mesh elements. All results from meshes with more than 12,278 elements were well converged; hence, 12,278 elements were selected for all simulations.

3.2. Model verification

In order to validate the model, the numerically predicted performance of the VRFB with no flow field was verified against the published validated work [29] at the same operating conditions. In Figure 2b, the simulated cell voltage during charging is depicted at various state of charge levels (SOC 0.15–0.95) under a galvanostatic applied current density of 60 mA·cm^{-2} and volumetric flow rate of 300 mL/min. It is evident that the three-dimensional model captures well the trend observed [29].

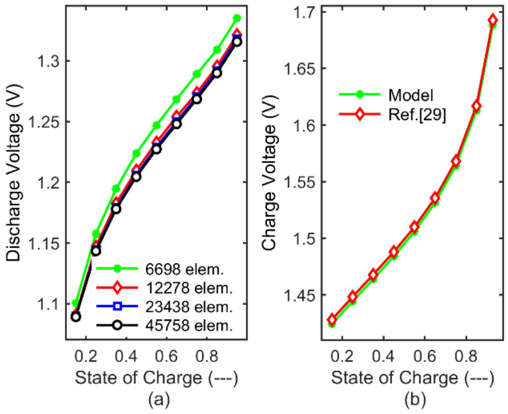

Figure 2. (a) Mesh independence of the discharge voltage at different SOC. (b) Comparison of simulated and numerical values of the charge voltage at a flow rate of 300 mL/min and current density of 60 mA/cm^2.

3.3. Effect of channel height on voltage response

Channel design is a crucial factor that affects battery performance in parallel with the flow rate and current density. In this section, three VRFB cells (cases 2, 5, and 8) were selected and simulated to show the effect of channel height on voltage response. They shared the same electrode thickness (4.5 mm) but at different channel heights (2, 1.5, and 1 mm), as listed in Table 1. Figure 3a shows the discharge voltage and the corresponding overpotential at SOC = 0.55 and current density 133.33 mA/cm^2 as the flow rate increased from 5 to 125 mL/min. It is clear that increasing the flow rate enhanced the output discharge voltage due to a decrease in the corresponding overpotential on the cathode side.

The improved voltage response was mainly affected by supplying ionic species to the porous electrode. It was dominated by either a convective diffusion process (at low flow rate conditions) or other parameters, rather than by diffusion mass transfer, such as reactive surface area and reactivity of the electrode (at high flow rate conditions).

The channel height impact on discharge voltage enhancement for cases 2, 5, and 8 is shown in Figure 3a. The cell with lower channel height (case 8) shows better voltage response when the inlet flow rate is low. Extra ionic species can reach the reaction sites in a porous electrode at high inlet velocity conditions, i.e., small inlet cross-sectional area.

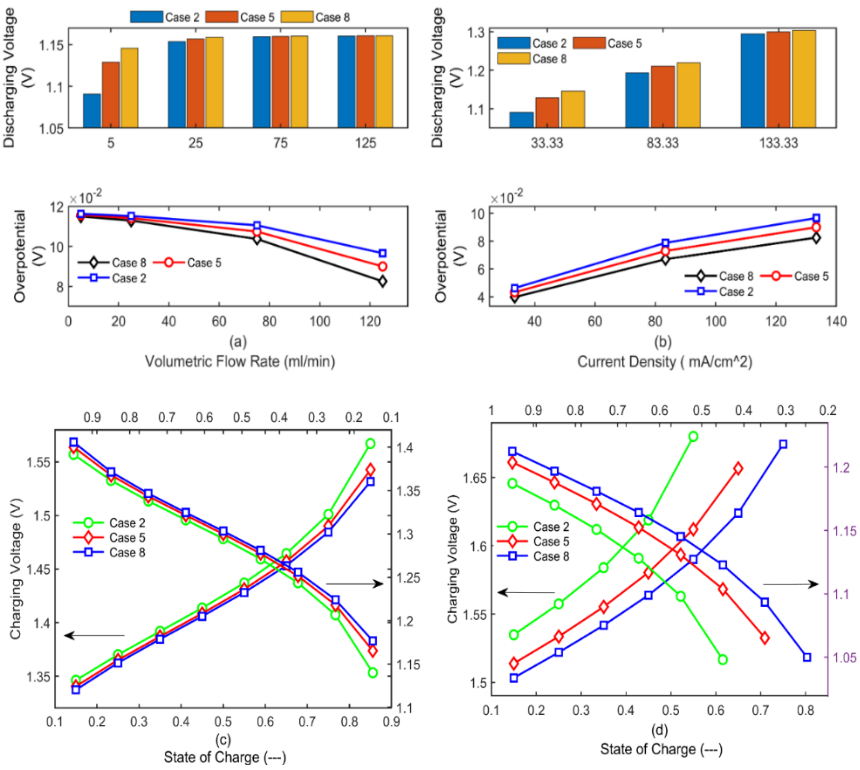

Figure 3. Impact of channel height on discharging voltage and overpotential at SOC = 0.55 and different (a) flow rates, (b) current densities, and (c, d) charge-discharge curves and discharging at 5 mL/min flow rate and current densities of 83.33 mA/cm^2 and 133.33 mA/cm^2, respectively.

However, with the increment in flow rate, this difference in voltage enhancement diminished because the performance was dominated by other factors, as referred, rather than by the diffusion ion transfer. Also, the voltage response was evaluated at a range of current densities (33.33, 83.33, 133.33 mA/cm^2) at SOC = 0.55 and volumetric flow rate of 5 mL/min. In Figure 3b, a high current density leads to an overpotential increment and a quick jump in voltage response during the charge process due to the elevated ohmic resistance, regardless of the supplied amount of flow rate. In general, there was an overpotential reduction as the channel height decreased, which led to higher cell voltage. Moreover, an increment in cell voltage was observed as the flow rate increased; the opposite was noticed as the current density increased.

Figures 3a and b demonstrate that the impact of channel height becomes more effective at conditions of low flow rate (low inlet velocity) and high current density (more electrolyte consumption). This fact was noticed in the cell (case 8) where more species can be provided into the electrodes since it has less cross-section area inlet (high pressure difference and velocity), as shown in Figure 6a (Section 3.5). Also, more species can be penetrated along the entire porous region (see

Table 3 in Section 3.5), and then more electrochemical reaction rates (voltage improvement) occur.

Figures 3c and d display the influence of the channel height on charge-discharge curves at a 5 mL/min flow rate and a constant current density (c: 83.33 mA/cm^2 and d: 133.33 mA/cm^2). In all figures with charge-discharge curves, the left-directed arrow refers to the charge process (left y-axis and bottom x-axis), while the right-directed arrow refers to the discharge process (right y-axis and top x-axis). Increasing SOC required more consumption of the electrolyte, which in turn enhanced voltage and related capacity. Also, as indicated in Figures 3a and b, case 8 displays better voltage response than cells in cases 5 and 2, specifically at high current density (Figure 3d), since applying high current density requires an extra amount of species (or high inlet flow velocity), which can be achieved by the cell in case 8 due to its smaller inlet cross-sectional area. It is important to note that terminal conditions may not be reached at specific operating conditions (low flow rate and/or high current density) due to concentration polarization. For instance, the charge and discharge voltages for the cell in case 2 at 5 mL/min were 1.7 and 0.1 V at SOCs 0.55 and 0.5 instead of 0.95 and 0.15, respectively, as shown in Figure 3d.

3.4. Effect of electrode thickness on voltage response

Electrode thickness is another key parameter affecting the VRFB performance. Three VRFB cells (cases 4, 5, and 6) were selected to show the effect of electrode thickness on voltage response. They shared the same channel height (1.5 mm) at different electrode thicknesses (6, 4.5, and 3 mm), as listed in Table 1. Regardless of electrode thickness, and at the same operating conditions as those applied in Section 3.3, there was an enhancement in output discharge voltage as the flow rate increased due to the decrease in corresponding overpotential, as shown in Figure 4a. However, a quick jump and drop in charge-discharge voltages and corresponding overpotentials were obtained as current density increased, as shown in Figure 4b. According to the obtained results, case 4 showed better voltage response than cases 5 and 6, which can be attributed to the fact that larger electrodes (case 4) involve more inner interaction sites for electrochemical reactions, which, in turn, promote electron transfer and enhance vanadium ion transfer. In general, a lower overpotential and a higher cell voltage were observed as electrode thickness increased, as shown in Figure 4a and b. Moreover, results demonstrate that cell 4, which was the best cell in this section, performed better than cell 8, the best option in Section 3.3, in terms of voltage response and corresponding overpotential at the same operating conditions. The reduction in overpotential presented in Figures 3a, b and 4a, b was positively affected by electrode thickness, more than by channel height, at the same operating conditions, which explains why cell 4 performed better than cell 8.

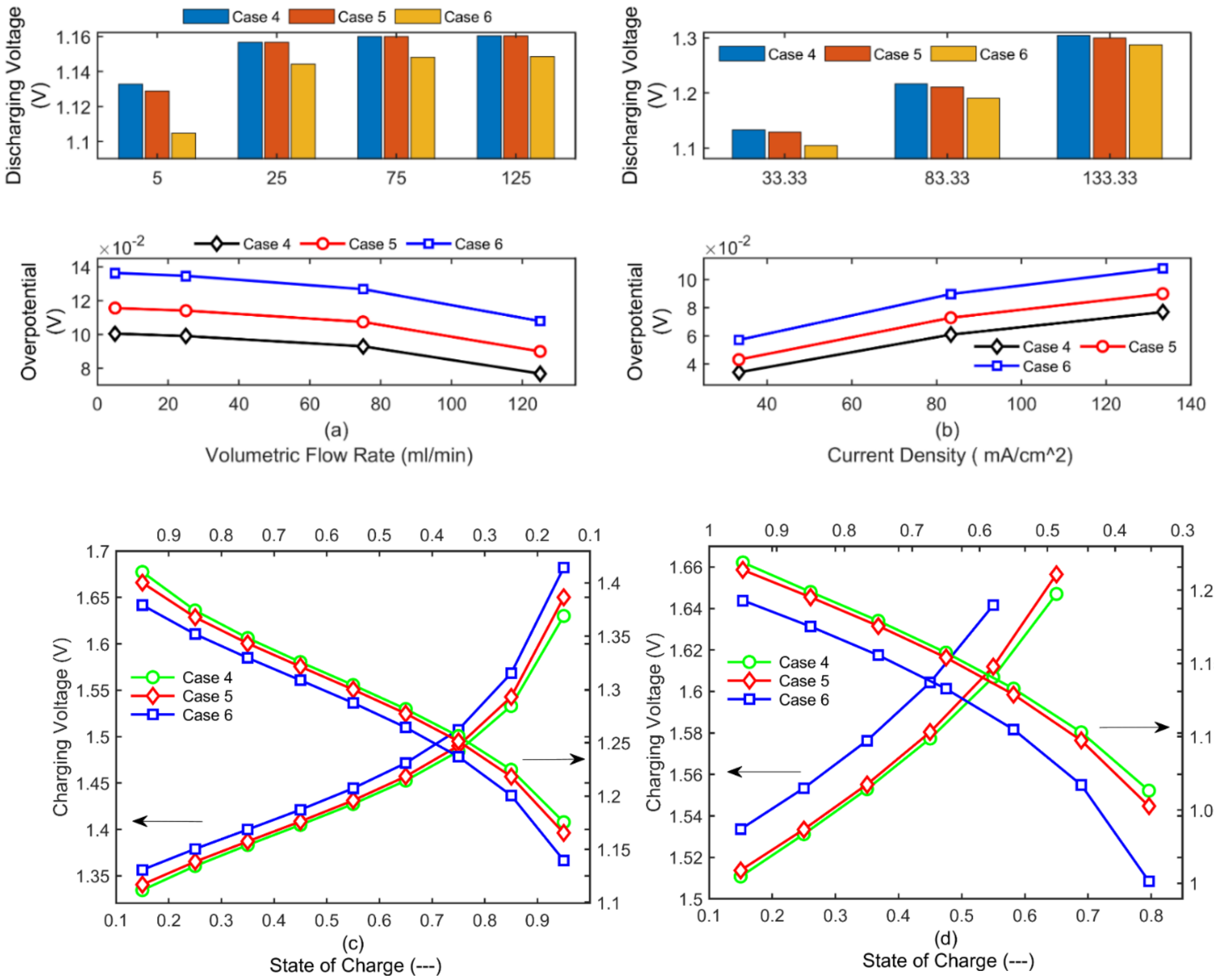

Figure 4. Impact of electrode thickness on discharging voltage and overpotential at SOC = 0.55 and different values of (a) flow rates, (b) current densities, and (c, d) charge-discharge curves at 5 mL/min flow rate and current densities of 83.33 mA/cm^2 and 133.33 mA/cm^2, respectively.

3.5. Dual impact of electrode thickness and channel height on voltage response

Nine combinations of a VRFB cell at different electrode thicknesses and channel heights (listed in Table 1) were simulated to reveal their dual impact on discharge voltage behavior at a 5 mL/min flow rate, SOC = 0.45, and 133.33 mA/cm^2 current density, as illustrated in Figure 5a. Based on the applied operating conditions, the best performance in terms of output voltage response was observed by the cell with 6 mm electrode thickness and 1 mm channel height (case 7), while the cell with 3 mm electrode thickness and 2 mm channel height (case 3) was the worst. The whole charge-discharge cycle along SOC was performed at 5 mL/min and 133.33 mA/cm^2 to recognize the general behavior of the nine studied cases, as shown in Figure 5b. Voltage response varied from best to worst in the following order: cases 7, 8, 9, 4, 5, 6, 1, 2, and 3. This sequence was mainly related to the actual amount of penetrated electrolyte into the porous electrode of each case. To obtain the actual transport of electrolyte to the porous electrode, a volume ratio (V_R) [volume of penetrated flow rate (V_P) to the actual volume of supplied flow rate (V_S)] at the channel inlet was defined as follows:

$$V_R = \frac{V_P}{V_S} \tag{24}$$

where V_P is calculated by the integration of average velocity (V_C) in the cathode electrode along its length (L), as follows [38]:

$$V_P = W_E \int_0^L V_C \, dL \tag{25}$$

where W_E is the width of the electrode, and L is the height of the electrode. Table 3 lists the volume ratios of the nine combinations; as expected, the volume ratio amount was directly proportional to the mentioned cell's sequence performance, i.e., the sequence of V_R amount for the cells.

Table 3. Volume ratio of electrolyte penetration into the cathode of nine cells under various flow rates.

Studied cases	**Volumetric flow rate (mL/min)**			
	5	25	75	125
	Electrolyte penetration ratio (%)			
Case 1	12.51	15.17	20.09	22.28
Case 2	10.34	12.84	17.73	19.82
Case 3	7.69	9.90	14.46	16.37
Case 4	21.00	23.36	27.81	29.89
Case 5	17.95	20.36	25.03	27.08
Case 6	13.94	16.34	21.11	23.02
Case 7	35.56	36.88	40.85	42.94
Case 8	32.33	33.59	37.40	39.34
Case 9	27.42	28.73	32.50	34.09

To understand why cells were ordered in this sequence, the nine cells were divided into two sets. The cells in set 1 were selected to share the same channel height at different electrode thicknesses, while the cells in set 2 were at the same electrode thickness and different channel heights. The first set involves groups A, B, and C, where each group represents cases 7, 8, and 9, cases 4, 5, and 6, and cases 1, 2, and 3, respectively. The second set involves groups D, E, and F, representing cases 1, 4, and 7, cases 2, 5, and 8, and cases 3, 6, and 9, respectively. In the first set, it was observed that the cell with higher electrode thickness, i.e., cell 7 in group A, cell 4 in group B, and cell 1 in group C, showed better charge-discharge voltage response than the others in the same group. Also, in set two, i.e., at a fixed electrode thickness (various channel heights), it was obvious that the cells with lower channel height in each group, i.e., cell 7 in group D, cell 8 in group E, and cell 9 in group F, showed better performance than the others in the same group, as displayed in Figure 5a. It can be concluded that reducing channel height and increasing electrode thickness enhances the voltage response. Also, the impact of channel height on cell voltage response improvement surpasses that of electrode thickness, depending on the operating conditions and cell geometry. For instance, in group A, cases 7, 8, and 9 behave better than the corresponding cells in groups B and C, since they have less channel height (1 mm), reflecting the importance of channel height, as shown in Figure 5 and discussed in Figure 3. At the same time, cell 7 shows a higher discharge voltage response than cases 8 and 9 in group A, due to its larger electrode thickness, which reflects the importance of electrode thickness, as discussed in Figure 4.

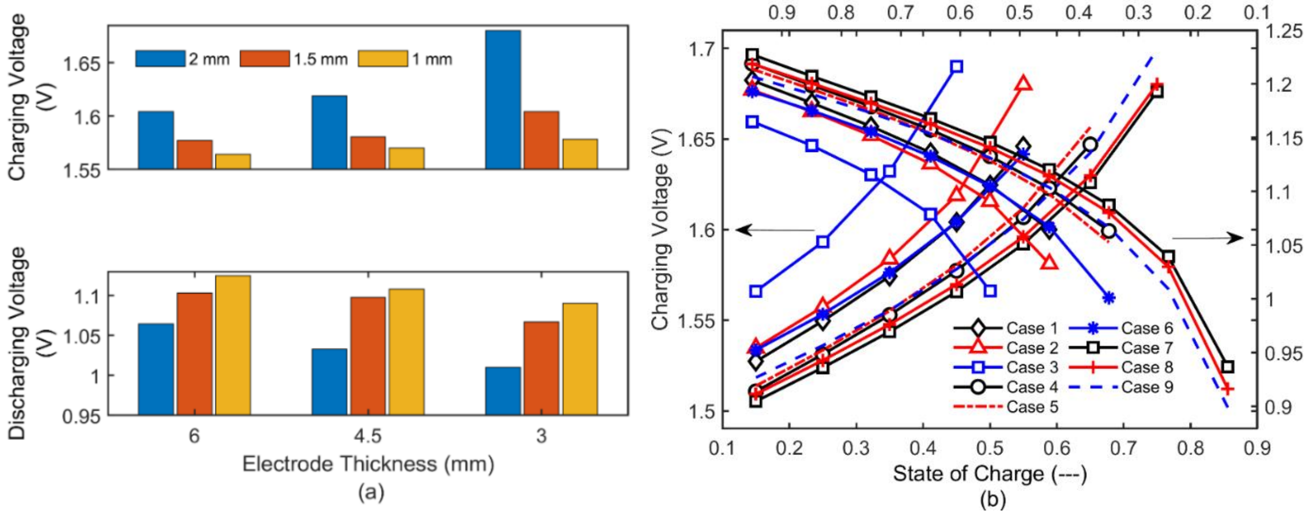

Figure 5. Dual impact of channel height and electrode thickness on charge-discharge voltages at 5 mL/min and 133.33 mA/cm^2: (a) SOC = 0.45; (b) different SOCs.

3.6. Overall battery performance

To evaluate the overall VRFB performance, a balance is required between pumping power losses and energy efficiency. Minimizing the energy for pumping flow rate (pumping power losses) and maximizing the energy conversion during charge-discharge cycles enhances overall battery efficiency. The pumping power can be defined as follows [20]:

$$P_m = \frac{2.V_S.\,\Delta p_{el}}{0.85} \tag{26}$$

where P_m, V_S, and Δp_{el} refer to the pumping power (W), volumetric flow rate (m^3/s), and pressure difference (Pa), respectively, whereas the numbers 2 and 0.85 refer to the two pumps and their efficiency. Since a steady-state condition is assumed in this model with no side reactions and species penetration through the membrane, the Coulombic efficiency is considered 100%. This assumption means that both energy (η_{En}) and voltage efficiencies are equal. Also, battery efficiency (η_{Ba}) as a function of SOC can be expressed as follows :

$$\eta_{En} = \frac{\int V_{dis} \times I_{dis}\ dSOC}{\int V_c \times I_c \quad dSOC} \tag{27}$$

$$\eta_{Ba} = \frac{\int (P_{dis}^{out} - P_m)\, dSOC}{\int (P_c^{in} + P_m)\ \ dSOC} \tag{28}$$

where the symbols (*c-dis, V, I, P, c, dis, out, in*) refer to the charge-discharge process, voltage, current, power, output, and input, respectively.

Figure 6a, b, and c depict the inlet channel velocity, pressure drop, and pumping power for the nine combinations as a function of flow rate. Pressure drop varies linearly against flow rates, whereas pumping power acts in a nonlinear manner [20]. It is obvious that cells in group A (cases 7, 8, and 9) demonstrate higher inlet velocity and corresponding pressure drop and pumping power compared to the cells in group B (cases 4, 5, and 6) and group C (cases 1, 2, and 3), since they have a lower channel height (1 mm), as listed in Table 1.

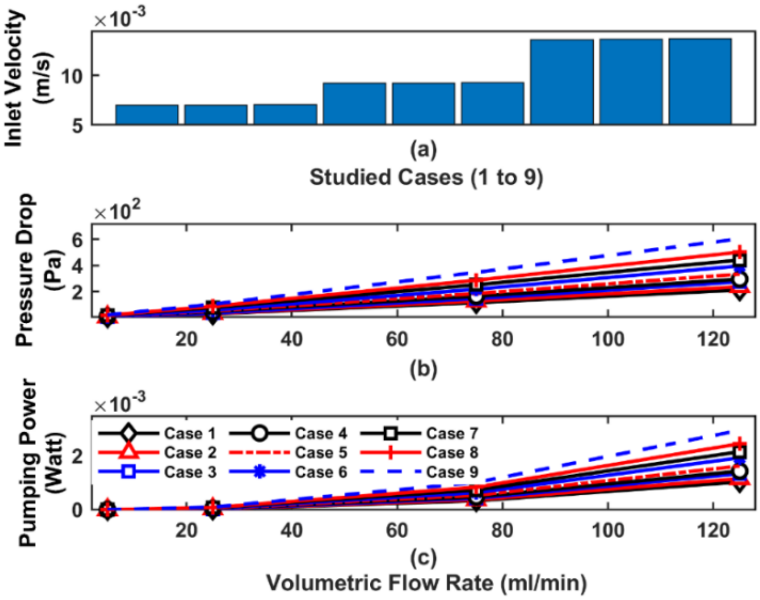

Figure 6. (a) Inlet velocity (m/s), (b) pressure drop (Pa), and (c) pumping power losses (W) of the nine cells at different flow rates.

High energy efficiency required in energy storage applications. Energy and battery efficiencies were calculated and analyzed under various operating conditions based on Eqs (27) and (28). In all studied cases, there was a gradual improvement in energy efficiency as the flow rate increased due to an enhancement in discharge voltage, as shown in Figures 3a and 4a. Figure 7a illustrates that case 7 represents the most efficient cell, whereas case 3 is the worst. Energy efficiency was mainly affected by the flow rate. At a low flow rate condition, the major role in finding energy efficiency was related to channel height; however, at a moderate or high flow rate, the opposite occurred, where electrode thickness dominated the energy efficiency magnitude. For instance, at a 5 mL/min flow rate and 33.33 mA/cm^2 current density, energy efficiencies were 91.8%, 91%, and 89.7% for group A, 91.4%, 90.6%, and 89.1% for group B, and 91.2%, 90.1%, and 88% for group C. The cells in group 1 were the most efficient since they had the smallest channel height (major role), i.e., 1 mm for group A, 1.5 mm for group B, and 2 mm for group C. Although cell 7 shares the same channel height as cells 8 and 9 in group A, it performs better due to its large electrode thickness (6 mm; minor role). However, there was almost no impact of channel height on energy efficiency at moderate or high flow rates, where efficiency was mainly controlled by electrode thickness. For instance, energy efficiency at a flow rate higher than 25 mL/min, regardless of channel height, was 92.2% for cells in group D (cases 7, 4, and 1) at 6 mm electrode thickness, 91.6% for cells in group E (cells 8, 5, and 2) at 4.5 mm electrode thickness, and 90.2% for cells in group F (cells 9, 6, and 3) at 3 mm electrode thickness, which reflects the role of electrode thickness on energy efficiency calculation.

Energy efficiency behavior under different current densities at a 5 mL/min flow rate is presented in Figure 7b. As discussed in the previous section for Figures 3d and 4d, increasing current density results in a quick jump/drop of charge/discharge voltages, leading to energy efficiency reduction due to the elevated ohmic resistance. Results indicated that the most efficient cell in terms of energy efficiency was case 7 (91.7%, 81%, and 72.1%) at current densities of 33.33, 83.33, and 133.33 mA/cm^2, respectively, and case 3 (88%, 73.3%, and 61.1%) at the same current densities.

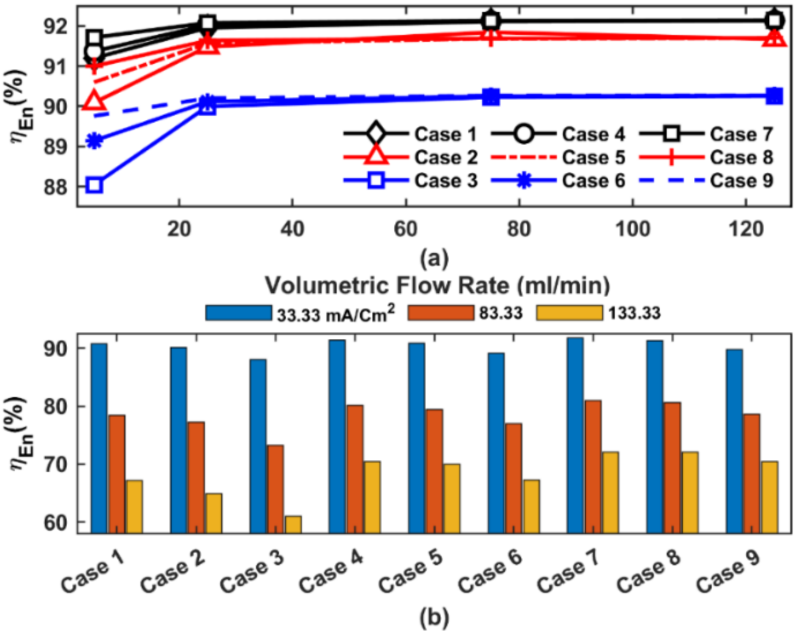

Figure 7. Energy efficiency of the nine cells at different (a) flow rates and 33.33 mA/cm^2, and (b) current densities and 5 mL/min.

Figure 8a illustrates the battery efficiency against volumetric flow rate at a current density of 33.33 mA/cm^2. In Figure 8a, the overall battery efficiency increases with flow rate until a specific maximum value (representing the optimal flow rate), then it declines as the flow rate passes its optimal magnitude, since pumping power losses overcomes the enhancement in voltage response, as stated in Eq (28). According to Figure 8a, the maximum efficiency at the optimal flow rate of 25 mL/min is 92%, 91.96%, 91.92%, 91.52%, 91.5%, 91.44%, 90.07%, 90.04%, and 89.95% for the cell cases 7, 4, 1, 8, 5, 2, 9, 6, and 3, respectively. It can be seen that cell 7 is the most efficient one, while cell 3 is the least efficient, as explained before. At low flow rates, battery efficiency behaves in a similar way to what was discussed for energy efficiency, i.e., channel height controls the performance more than does the electrode thickness, since pumping losses are relatively small, while at moderate and high flow rates, the electrode thickness dominates the performance. Although cell cases 7, 8, and 9 in group A (1 mm channel height) exhibited the highest performance in terms of battery efficiency at optimal and low flow rates, they behaved in the opposite direction at high flow rates, since they suffered from higher pressure drop compared to others, as depicted in Figure 6. The effect of various current densities on overall battery efficiency at 5 mL/min is demonstrated in Figure 8b, where high ohmic resistance and concentration polarization occurred as the flow rate increased, which is in line with what was discussed earlier.

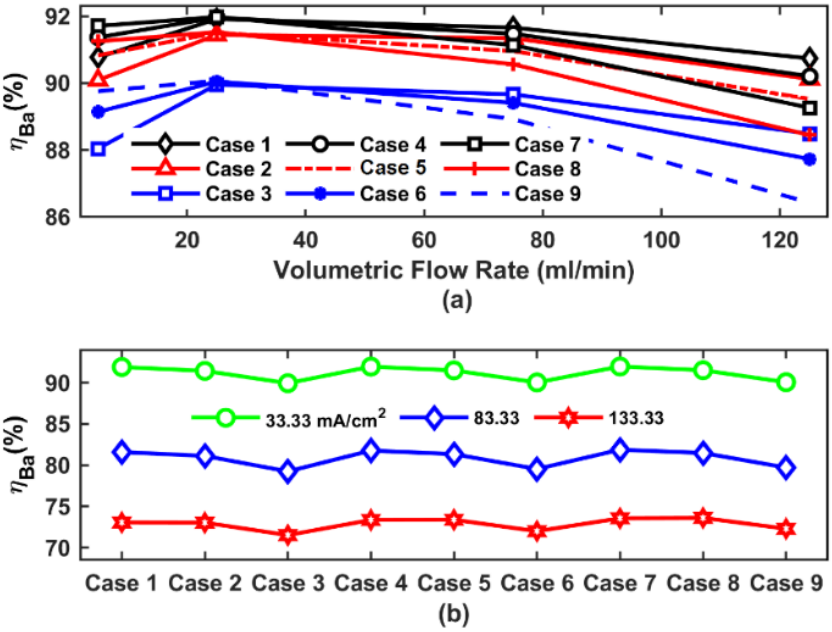

Figure 8. Battery efficiency of the nine cells at different (a) flow rates and 33.33 mA/cm^2 and (b) current densities and 5 mL/min.

Table 4. Overall battery efficiency of the nine cells under different operating conditions.

Current density (mA/cm^2)	**Flow rate (mL/min)**	**Battery efficiency**								
		Case 1	Case 2	Case 3	Case 4	Case 5	Case 6	Case 7	Case 8	Case 9
33.33	5	90.77%	90.09%	88.04%	91.37%	90.83%	89.14%	91.71%	91.25%	89.76%
	25	91.92%	91.44%	89.95%	91.96%	91.50%	90.04%	91.98%	91.52%	90.07%
	75	91.66%	91.34%	89.66%	91.48%	90.96%	89.41%	91.14%	90.56%	88.93%
	125	90.74%	90.12%	88.49%	90.20%	89.52%	87.73%	89.26%	88.44%	86.42%
83.33	5	78.43%	77.21%	73.29%	80.12%	79.43%	76.95%	80.99%	80.56%	78.62%
	25	81.59%	81.13%	79.25%	81.77%	81.34%	79.54%	81.88%	81.48%	79.71%
	75	81.84%	81.40%	79.62%	81.80%	81.37%	79.57%	81.70%	81.25%	79.43%
	125	81.55%	81.08%	79.24%	81.37%	80.87%	78.99%	81.04%	80.49%	78.54%
133.33	5	67.19%	64.93%	61.02%	70.50%	70.02%	67.31%	72.06%	72.05%	70.44%
	25	73.05%	73.03%	71.51%	73.36%	73.38%	72.00%	73.56%	73.61%	72.25%
	75	73.63%	73.63%	72.30%	73.64%	73.65%	72.33%	73.68%	73.62%	72.28%
	125	73.50%	73.50%	72.16%	73.41%	73.40%	72.03%	73.24%	73.20%	71.79%

Table 4 displays the battery efficiency at different flow rates and current densities. It can be seen that the best efficiency was achieved either by cell case 7 at flow rates equal to or less than the optimal value or by cell case 1 at flow rates higher than the optimal value. To evaluate the impact of channel height and electrode thickness on overall battery performance, the efficiency at optimal flow rate (which is not constant) was determined and highlighted for each current density, as shown in Table 3. Since the battery efficiency in cell cases 4, 1, 8, and 9 was closer to cell case 7, their performance was analyzed and compared to the reference cell (case 7). In Table 4, at a low current density (33.33 mA·cm^2), the optimal flow rate is 25 mL/min, at which cell cases 1 and 4 are closer to cell case 7 than cell cases 8 and 9, and cell case 4 performs slightly better than cell case 1: 91.96% vs. 91.92%. However, at higher current densities, the optimal flow rate is not constant anymore (i.e., increased) due to the increment in species consumption, where cell cases 1 and 4 are still closer to cell 7 at smaller differences. Overall, since cell cases 7, 4, and 1 in group D show the best performance, evaluating overall battery efficiency starts with electrode thickness (6 mm), followed by channel height, based on the applied operating conditions and geometry design.

4. Conclusions

In this study, a 3D steady-state numerical model was developed and implemented to reveal the dual effect of channel height and electrode thickness of a single VRFB cell. The work focused on discovering the relationship between flow rate, SOC, and current density, along with electrode thickness/channel height and battery performance, including charge-discharge voltage responses and energy/overall battery efficiency. For all combinations, during the charge-discharge cycle, fast flow rates enhanced electrochemical responses while also negatively affecting overall battery efficiency due to pumping power losses. As a result, energy efficiency improved gradually with increased flow rate, whereas overall efficiency first increased and then decreased due to large pump losses. The battery performance became noticeable as channel height decreased and electrode thickness increased. Also, at low flow rate conditions, channel height determined battery performance, more than did electrode thickness; however, the opposite was true at moderate and high flow rates. For the nine selected combinations, the optimal flow rate was not constant as the current density increased. Overall, energy and battery efficiency were mainly affected by electrode thickness more than by channel height based on the operating conditions and cell geometry. Also, among the studied cases, cell case 7 (6 mm electrode thickness, 1 mm channel height) was best in terms of energy/battery efficiency. On the other hand, cell case 3 (3 mm electrode thickness, 2 mm channel height) was the worst; however, this advantage became lower at higher current densities. This model is applicable to study the effect of other electrode physical properties such as porosity and flow field architectures of many flow batteries.

Use of AI tools declaration

The author declares he has not used Artificial Intelligence (AI) tools in the creation of this article.

Conflicts of interest

The author declares no conflicts of interest in this paper.

References

1. Bashiru O, Ochem C, Enyejo LA, et al. (2024) The crucial role of renewable energy in achieving the sustainable development goals for cleaner energy. *Global J Eng Technol Adv* 19: 011–036. https://doi.org/10.30574/gjeta.2024.19.3.0099

2. Deshmukh MKG, Sameeroddin M, Abdul D, et al. (2023) Renewable energy in the 21st century: A review. *Mater Today: Proc* 80: 1756–1759. http://dx.doi.org/10.1016/j.matpr.2021.05.501
3. Hoang AT, Nguyen XP (2021) Integrating renewable sources into energy system for smart city as a sagacious strategy towards clean and sustainable process. *J Cleaner Prod* 305: 127161. http://dx.doi.org/10.1016/j.jclepro.2021.127161
4. Li J, Al-Yasiri M, Pham H, et al. (2024) Chapter 10–Redox flow batteries. In: Thomas S, Rouxel D, Kalarikkal N, et al., (editors), *Advanced Materials for Battery Separators*, Elsevier, 327–347 https://doi.org/10.1016/B978-0-12-817507-1.00003-X
5. Arévalo-Cid P, Dias P, Mendes A, et al. (2021) Redox flow batteries: A new frontier on energy storage. *Sustainable Energy Fuels* 5: 5366–5419. http://dx.doi.org/10.1039/D1SE00839K
6. Soloveichik GL (2015) Flow batteries: Current status and trends. *Chem Rev* 115: 11533–11558. http://dx.doi.org/10.1021/cr500720t
7. Petrov MM, Modestov AD, Konev DV, et al. (2021) Redox flow batteries: Role in modern electric power industry and comparative characteristics of the main types. *Russ Chem Rev* 90: 677. http://dx.doi.org/10.1070/RCR4987
8. Park J, Al-Yasiri MA (2019) Distributed energy storage system. Available from: https://mst.elsevierpure.com/ws/portalfiles/portal/41548194/Distributed%20energy%20storage%20system.pdf.
9. Li Y, Vankelecom I (2017) Nonaqueous redox flow batteries. *Redox Flow Batteries*: CRC Press, 373–401. http://dx.doi.org/10.1201/9781315152684-11
10. Du J, Lin H, Zhang L, et al. (2025) Advanced materials for vanadium redox flow batteries: Major obstacles and optimization strategies. *Adv Funct Mater,* 2501689. http://dx.doi.org/10.1002/adfm.202501689
11. Sharmoukh W (2025) Redox flow batteries as energy storage systems: Materials, viability, and industrial applications. *RSC Adv* 15: 10106–10143. http://dx.doi.org/10.1039/D5RA00296F
12. Akuzum B, Alparslan YC, Robinson NC, et al. (2019) Obstructed flow field designs for improved performance in vanadium redox flow batteries. *J Appl Electrochem* 49: 551–561. http://dx.doi.org/10.1007/s10800-019-01306-1
13. Huang Z, Mu A (2021) Flow field design and performance analysis of vanadium redox flow battery. *Ionics* 27: 5207–5218. http://dx.doi.org/10.1007/s11581-021-04213-8
14. Xiao W, Tan L (2019) Control strategy optimization of electrolyte flow rate for all vanadium redox flow battery with consideration of pump. *Renewable Energy* 133: 1445–1454. http://dx.doi.org/10.1016/j.renene.2018.09.018
15. Saha S, Maniam KK, Paul S, et al. (2023) Hydrodynamic and electrochemical analysis of compression and flow field designs in vanadium redox flow batteries. *Energies* 16: 6311. http://dx.doi.org/10.3390/en16176311
16. Ma X, Zhang H, Sun C, et al. (2012) An optimal strategy of electrolyte flow rate for vanadium redox flow battery. *J Power Sources* 203: 153–158. http://dx.doi.org/10.1016/j.jpowsour.2011.11.036
17. Lu M-Y, Deng Y-M, Yang W-W, et al. (2020) A novel rotary serpentine flow field with improved electrolyte penetration and species distribution for vanadium redox flow battery. *Electrochim Acta* 361: 137089. http://dx.doi.org/10.1016/j.electacta.2020.137089

18. Wang Q, Qu Z, Jiang Z, et al. (2018) Experimental study on the performance of a vanadium redox flow battery with non-uniformly compressed carbon felt electrode. *Appl Energy* 213: 293–305. http://dx.doi.org/10.1016/j.apenergy.2018.01.047
19. Rao P, Jayanti S (2021) Influence of electrode design parameters on the performance of vanadium redox flow battery cells at low temperatures. *J Power Sources* 482: 228988. https://doi.org/10.1016/j.jpowsour.2020.228988
20. Al-Yasiri MA (2020) A parametric analysis of the output voltage of all-vanadium redox-flow battery system. *IOP Conference Series: Materials Science and Engineering* 871: 012007. http://dx.doi.org/10.1088/1757-899X/871/1/012007
21. Maurya S, Nguyen PT, Kim YS, et al. (2018) Effect of flow field geometry on operating current density, capacity and performance of vanadium redox flow battery. *J Power Sources* 404: 20–27. http://dx.doi.org/10.1016/j.jpowsour.2018.09.093
22. Messaggi M, Canzi P, Mereu R, et al. (2018) Analysis of flow field design on vanadium redox flow battery performance: Development of 3D computational fluid dynamic model and experimental validation. *Appl Energy* 228: 1057–1070. http://dx.doi.org/10.1016/j.apenergy.2018.06.148
23. Gundlapalli R, Jayanti S (2019) Effect of channel dimensions of serpentine flow fields on the performance of a vanadium redox flow battery. *J Energy Storage* 23: 148–158. http://dx.doi.org/10.1016/j.est.2019.03.014
24. Park J, Al-Yasiri MA (2021) Cell for flow battery. Google Patents. Available from: https://scholarsmine.mst.edu/mec_aereng_facwork/4417/.
25. Liu X, Zhang P, Yang J, et al. (2023) Effect of variable cross-section electrode on the battery performance of all-vanadium redox flow battery. *Int J Heat Mass Transfer* 215: 124382. https://doi.org/10.1016/j.ijheatmasstransfer.2023.124382
26. Zheng Q, Xing F, Li X, et al. (2015) Dramatic performance gains of a novel circular vanadium flow battery. *J Power Sources* 277: 104–109. https://doi.org/10.1016/j.jpowsour.2014.11.142
27. Ali E, Kwon H, Choi J, et al. (2020) A numerical study of electrode thickness and porosity effects in all vanadium redox flow batteries. *J Energy Storage* 28: 101208. https://doi.org/10.1016/j.est.2020.101208
28. Al-Yasiri MA (2022) Predicting the maximum output current and potential voltage response of a vanadium redox flow battery. *AIP Conf Proc* 2386: 040015. http://dx.doi.org/10.1063/5.0066857
29. Al-Yasiri MA (2020) Enhancing the vanadium redox flow battery efficiency by adjusting the electrode configuration. *AIMS Energy* 8: 771. http://dx.doi.org/10.3934/energy.2020.5.771
30. Chai Y, Qu D, Fan L, et al. (2024) A double-spiral flow channel of vanadium redox flow batteries for enhancing mass transfer and reducing pressure drop. *J Energy Storage* 78: 110278. http://dx.doi.org/10.1016/j.est.2023.110278
31. Xiong B, Li Y, Ding Y, et al. (2023) Numerical analysis of vanadium redox flow batteries considering electrode deformation under various flow fields. *J Power Sources* 564: 232814. https://doi.org/10.1016/j.jpowsour.2023.232814
32. You D, Zhang H, Chen J (2009) A simple model for the vanadium redox battery. *Electrochim Acta* 54: 6827–6836. https://doi.org/10.1016/j.electacta.2009.06.086
33. Xu Q, Zhao TS, Leung PK (2013) Numerical investigations of flow field designs for vanadium redox flow batteries. *Appl Energy* 105: 47–56. https://doi.org/10.1016/j.apenergy.2012.12.041

34. Zhu S, Pelton RH, Collver K (1995) Mechanistic modelling of fluid permeation through compressible fiber beds. *Chem Eng Sci* 50: 3557–3572. https://doi.org/10.1016/0009-2509(95)00205-J
35. Ma X, Zhang H, Xing F (2011) A three-dimensional model for negative half cell of the vanadium redox flow battery. *Electrochim Acta* 58: 238–246. https://doi.org/10.1016/j.electacta.2011.09.042
36. Shah AA, Watt-Smith MJ, Walsh FC (2008) A dynamic performance model for redox-flow batteries involving soluble species. *Electrochim Acta* 53: 8087–8100. https://doi.org/10.1016/j.electacta.2008.05.067
37. Sukkar T, Skyllas-Kazacos M (2003) Water transfer behaviour across cation exchange membranes in the vanadium redox battery. *J Membr Sci* 222: 235–247. http://dx.doi.org/10.1016/S0376-7388(03)00309-0
38. Ke X, Alexander JID, Prahl JM, et al. (2015) A simple analytical model of coupled single flow channel over porous electrode in vanadium redox flow battery with serpentine flow channel. *J Power Sources* 288: 308–313. http://dx.doi.org/10.1016/j.jpowsour.2015.04.138

AIMS Press